Towards a Protein-Size Dependent Resolution Limit due to Dynamical Scattering in Cryo-transmission Electron Microscopy

Max Leo Leidl, Sebastian Sturm, Aikaterina Filopoulou, Carsten Sachse, Knut Müller-Caspary

Microscopy and Microanalysis, 2025, **31**, ozaf123
https://doi.org/10.1093/mam/ozaf123
Advance access publication 24 December 2025
Original Article

PICO 2024 Celebrating 20 Years of the ER-C

Microscopy AND Microanalysis

Towards a Protein-Size Dependent Resolution Limit due to Dynamical Scattering in Cryo-transmission Electron Microscopy

Max Leo Leidl[1,2], Sebastian Sturm[1], Aikaterina Filopoulou[2,3], Carsten Sachse[2,3], and Knut Müller-Caspary[1,*]

[1]*Department of Chemistry and Center for NanoScience, Ludwig-Maximilians-University Munich, Butenandtstr. 11, Munich 81377, Germany*
[2]*Ernst-Ruska Centre for Microscopy and Spectroscopy with Electrons (ER-C-3/Structural Biology), Forschungszentrum Jülich GmbH, Jülich 52425, Germany*
[3]*Department of Biology, Heinrich Heine University Düsseldorf, Universitätsstr. 1, Düsseldorf 40225, Germany*

***Corresponding author:** Knut Müller-Caspary, E-mail: k.mueller-caspary@cup.lmu.de

Abstract

In cryo-transmission electron microscopy, single-particle reconstructions exploit the weak phase object approximation. A decisive aspect to be studied systematically is to what extent underlying scattering assumptions limit the resolution, whether theoretical limits are compatible with experimental observations, and if current experimental benchmarks achieve this limit. Single-, multislice, and hybrid scattering models are employed in this work for simulating eight protein complexes up to 97.5 nm in thickness, embedded in low-density amorphous ice obtained from molecular dynamics. With the multislice scheme providing an accurate solution to the multiple scattering problem as reference, the reliability of the different models is assessed in both real and Fourier space, particularly via Fourier ring correlations at the specimen exit wave level. A comparison with benchmarking literature resolutions is performed. Our results show proportionality of the attainable resolution to the square root of the projection thickness. This is in reasonable quantitative agreement with the highest resolution published experimentally for proteins with at least the size of apoferritin. The study provides a rationale for the expectable resolution for a protein complex of known size. The implications of structural noise due to the ice background for the minimal ice thickness on protein size-dependent resolution are discussed, as well as efficient methods to approximate multiple scattering and propagation in thick proteins.

Introduction

Cryo-transmission electron microscopy (cryo-TEM) has successfully resolved a multitude of different proteins with steadily increasing spatial resolution. For apoferritin, atomic resolution down to 1.22 Å has been achieved in Nakane et al. (2020) and Yip et al. (2020) in 2020, which recently improved to 1.09 Å Küçükoğlu et al. (2024). Considering 1.4 Å as a threshold for resolving atomic features, cryo-TEM currently reaches near-atomic resolution between 1.4 Å and 2.0 Å for a variety of proteins. While attaining atomic or near-atomic resolution is a challenge in terms of instrumental performance, vitrified specimen preparation, and 3D reconstruction software, resolution limits appear to be additionally dependent on protein size and type.

Furthermore, cryo-TEM data exhibit a low signal-to-noise ratio (SNR) due to the low electron dose that proteins can withstand. Consequently, thousands up to millions of particles are needed to push the SNR by aligning and averaging. The averaging is also required to fill the information gaps due to the oscillating contrast transfer function (CTF) resulting from the large defoci needed to convert the phase into amplitude contrast. Further aspects that impact the resolution limits are related to particle movement, conformational homogeneity or drift. Strategies such as dose fractionation and motion correction can mitigate some of these effects at least partly.

On the one hand, significant improvements in hardware and data processing were made in recent years (Rohou & Grigorieff, 2015; Punjani et al., 2017; Faruqi & McMullan, 2018; Zivanov et al., 2019, 2020). On the other hand, contemporary single-particle workflows explicitly assume the validity of single-scattering in terms of a phase object (PO) or weak phase object (WPO), respectively, to model the specimen exit wave. In addition, the WPO is implicitly utilized in processing steps that involve corrections of the Fourier coefficients of recorded images by means of the CTF.

In general, addressing the attainable spatial resolution in single-particle cryo-TEM is a multifaceted challenge that requires a careful and comprehensive analysis of protein flexibility, conformational homogeneity, detector characteristics, low-density amorphous (LDA) ice thickness, data processing strategies, electron dose, coherence aspects, charging of the specimen during acquisition, and the imaging process by the optical system. However, these effects can be categorized into specimen-specific, detection-related, and those dependent on the imaging process. Let us briefly assume that a sufficiently large number of classes can be determined that cover all possible conformations of a protein under study and that sufficient data has been collected such that the resolution of a reconstruction using the different classes is not dose-limited. Let the LDA ice be of ideal thickness and the data processing

Received: July 22, 2024. **Revised:** October 20, 2025. **Accepted:** November 20, 2025

be exact regarding the alignment of the individual images and projection angles. Consequently, the imaging process remains the primary limitation to attainable resolution. Thus, a fundamental question is whether these factors or additional aspects limit the achievable resolution given governing parameters such as protein size. In this respect, the present study assumes an idealized situation.

Two aspects are crucial: the quality of the electron optics and the preferably direct interpretability of the recorded images in terms of structural properties. Concerning the optics, modern microscopes provide sufficient point resolution, especially in the aberration-corrected era (Urban, 2008; Kabius et al., 2009). This means that real-space details of the exit wave are theoretically transferred to the image plane with sub-Angstrom spatial resolution. However, cryo-TEM imaging relies on large defoci to transfer phase information from the object plane to intensity variation in the image plane. This results in a low structural fidelity of the recorded images regarding the phase of the specimen exit wave, necessitating consideration of the imaging process in cryo-TEM reconstructions. Only at this stage do assumptions about the scattering model become central, especially when the exit wave is considered to represent the projected structure. To disentangle the effects of electron optics and interaction with the specimen at the level of image intensity or its Fourier transform, the weak phase approximation is typically involved to obtain closed-form expressions.

The present work elucidates model violations that occur when the experimental, complex exit wave formation via dynamical scattering is replaced by various single-scattering assumptions during the single-particle reconstruction workflow. In this sense, the resolution limits worked out here do not apply comprehensively to cryo-TEM but rather refer to exploiting, e.g., the WPO approximation in contemporary cryo-TEM image *processing*. For this purpose, we investigate the effect of multiple scattering and propagation on the attainable resolution for eight proteins of different sizes, embedded in LDA ice. These proteins are hemoglobin, erythrocyte catalase, apoferritin, tobacco mosaic virus (TMV), 70s ribosome, capsid of porcine bocavirus, 48 nm doublet microtubule from tetrahymena thermophila, hepatitis B virus capsids and rotavirus. The 48 nm doublet microtubule from tetrahymena thermophila and the hepatitis B virus capsid have nearly the same projection thickness. Therefore, only the 48 nm doublet microtubule from tetrahymena thermophila is used in the detailed analysis. The proteins cover a thickness between 6 nm and 97.5 nm when measured along electron beam direction. Single-slice, single-scattering and multislice simulations have been performed for one projection direction, and LDA ice with a realistic density and structure has been obtained by molecular dynamics simulations. The results are compared in real space as well as in Fourier space using the Fourier ring correlation (FRC). Since the multislice method represents elastic scattering in specimens with elevated thickness most accurately among the models studied here, FRCs are calculated using the multislice results as a reference for all single-scattering models. In particular, the first zero of the FRC is used as a criterion for the theoretical resolution limit for WPO and PO-based model assumptions, which is then compared to the highest resolution obtained experimentally as reported in the PDBe (Armstrong et al., 2020). To differentiate between propagation and multiple scattering, we furthermore studied the thick WPO (tWPO) (Seki et al., 2018), which accounts for the correct propagation to the specimen exit face after a scattering event but neglects multiple scattering, and compare it to the exit waves of the multislice simulations.

Theory

The multislice algorithm (Cowley & Moodie, 1957, 1959*a*, 1959*b*) describes the propagation of a wave through a medium by slicing the electrostatic potential created by the atoms into thin slices. The 3D potential of each slice is projected along the electron beam direction and applied as a phase factor (phase grating) to the electron wave incident on the respective slice at the slice center. In between the slice centers, the electron wave is propagated in potential-free space using the Fresnel propagator. To accurately account for dynamical scattering, slices as thin as a few Å are conveniently used. However, the required slice thickness needs to decrease with increasing atomic number, and depends on the crystallinity of the specimen. For proteins in LDA, a recent study (Leidl et al., 2023) has shown that much coarser slicings of a few nanometers can be used to accurately account for multiple scattering in biological matter.

In this work, we performed multislice simulations for the different specimens to take multiple scattering into account. The propagation from the exit plane of a slice to the center of the next slice is described by the convolution with the Fresnel propagator $F_{z/2}$ (Goodman, 2005). The wave at the exit face of slice n is then given by

$$\psi_{n+1} = F_{z/2} \otimes \left\{\varphi_n \cdot \left[F_{z/2} \otimes \psi_n\right]\right\}, \tag{1}$$

where $\varphi_n = \exp\left[\mathrm{i}\sigma V_n\right]$ contains the projected potential $V_n(\boldsymbol{r})$ of slice n, ψ_n is the entrance wave of slice n, and σ is the interaction constant. Note that equation (1) is valid in real space, and that the dependence of all functions on real space coordinate $\boldsymbol{r}$ has been omitted for reasons of compactness. In cryo-TEM, the incident wave $\psi_0(\boldsymbol{r}) = 1$ is a plane wave.

Assuming that the slices are thin enough to be approximated by the WPO, being the first-order Taylor expansion such that $\varphi_n(\boldsymbol{r}) \approx 1 + \mathrm{i}\sigma V_n(\boldsymbol{r})$, then ψ_{n+1} becomes

$$\psi_{n+1} = \psi_0 + F_{z/2} \otimes \left\{\mathrm{i}\sigma V_n \cdot \left[F_{z/2} \otimes \psi_n\right]\right\}. \tag{2}$$

Neglecting quadratic and higher order terms of V_n, the exit wave after N slices is given by

$$\psi_N = 1 + \mathrm{i}\sigma \sum_{n=1}^{N} F_{(N-n+\frac{1}{2})z} \otimes V_n, \tag{3}$$

where $N \cdot z$ is the total specimen thickness, such that $(N - n + \frac{1}{2})z$ is the distance from the center of slice n to the exit face of the specimen. $\psi_0 = 1$ was assumed due to plane wave incidence; however, formulating equation (3) for an arbitrary illumination, such as a focused probe, is straightforward. In this model, the incoming wave propagates to each slice center without being scattered before (thus remaining a plane wave in the case of cryo-TEM), the weak interaction with each slice is calculated, and the resulting wave is propagated to the exit surface of the specimen without further interaction. The scattered waves emerging from all slices are summed coherently to form the exit wave function. Although this model is a single-scattering approximation, the scattering is explicitly depth-dependent and happens at the correct coordinate along electron beam direction in the specimen. The model in equation (3) is known as the thick WPO approximation (tWPO) (Seki et al., 2018). It is similar to the approach described by

Table 1. Used Atomic Models and the Corresponding PDBe Entry and Simulation Details

Protein (PDBe)	Simulation cell (x/y/z) (nm)	Comparison cell (x/y) (nm)	Number of slices	Pixel size (Å)	Total structure weight (kDa)
Hemoglobin HbA complex (5ni1) Khoshouei et al. (2017)	24.93 × 24.93 × 6.0	6.62 × 6.92	16	0.015	64
Erythrocyte catalase (7p8w) Chen et al. (2022)	24.93 × 24.93 × 7.5	9.56 × 9.83	20	0.030	245
Apoferritin (7a6a) Yip et al. (2020)	24.94 × 24.94 × 13.5	12.40 × 12.40	36	0.061	511
Tobacco mosaic virus (6sag) Weis et al. (2019)	24.95 × 20.67 × 19.5	24.94 × 20.67	52	0.061	2499 (17)
70s ribosome (8b0x) Fromm et al. (2023)	64.74 × 64.74 × 24.0	25.72 × 21.91	64	0.079	2185
Capsid porcine bocavirus (8tu1) Velez et al. (2023)	64.74 × 64.74 × 28.5	27.12 × 27.12	76	0.158	3802
Doublet microtubule tetrahymena thermophila (8g3d) Kubo et al. (2023)	111.05 × 111.05 × 33.0	66.52 × 45.11	88	0.068	20362
Hepatitis B virus core shell (6tik) Aston-Deaville et al. (2020)	111.05 × 111.05 × 34.5	33.34 × 33.34	92	0.068	372.720
Rotavirus (4v7q) Settembre et al. (2011)	111.05 × 111.05 × 97.5	96.84 × 96.84	260	0.068	1440

For the tobacco mosaic virus, the molecular weight of an asymmetric unit is given in brackets.

DeRosier (2000) and Gureyev et al. (2020), except that equation (3) involves the *coherent* sum over waves from different depths in the specimen which is a fundamental difference. Since these waves interfere with each other before the imaging process, the resulting image may not necessarily be interpretable as the sum of separate TEM images arising from different specimen depths. The latter assumes that among the N interfering waves from different slices, only the N quadratic terms contribute to the image intensity, meaning that the additional $N^2 - N$ mixed terms are considered to be of minor importance. In that case, the model is equivalent to taking the curvature of the Ewald into account (DeRosier, 2000; Gureyev et al., 2020). This approach is routinely employed in cryo-EM reconstructions since it provides a direct relation between the specimen potential and the image intensities, such that data in this work is also compared with the Ewald correction model where appropriate.

Methods

The eight protein structures were taken from the Protein Data Bank in Europe (PDBe) (Armstrong et al., 2020) and embedded in LDA ice to account for the structural noise of the background. In all simulations, the ice was assumed to be as thin as possible, with a thickness that was a multiple of 15 Å. Molecular dynamics simulations using the LAMMPS software (Thompson et al., 2022) were used to calculate the atomic model of the LDA ice as described previously (Leidl et al., 2023). The ice cell was then combined with the atomic model of the proteins via binary masks that account for the hydration radius (Shang & Sigworth, 2012). Assuming a cubic box around the protein model loaded from the PDBe, the thinnest direction was aligned with the optical axis, i.e., the direction of the incident electron beam. Simulation parameters are listed in Table 1. For further details, we refer to ref. 28. For all proteins, we used equal slice thicknesses of $z = 3.75$Å being equivalent to one quarter of a single ice layer. Atomic scattering amplitudes from Lobato & Van Dyck (2014) were employed to generate the projected potentials of each slice. The object transfer functions of the PO and WPO approaches have been derived from the projected potential V by the sum of the potentials of all slices, yielding the phase and the imaginary part of the PO and WPO approximation, respectively:

$$\mathrm{PO} = e^{\mathrm{i}\cdot\sigma\cdot V}. \tag{4}$$

$$\mathrm{WPO} = 1 + \mathrm{i}\cdot\sigma\cdot V. \tag{5}$$

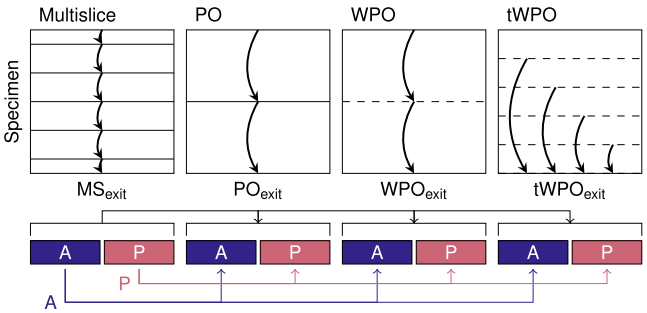

Fig. 1. Schematic explaining the different scattering models and their comparison. *Top:* Illustration of the multislice (MS), phase object (PO), weak phase object (WPO), and thick WPO (tWPO) scattering model. Solid lines indicate slice centers where the PO approximation is made, dashed lines refer to the WPO approach, and arrows denote Fresnel propagation. *Bottom:* Connections at the top (black) refer to the comparison of the full complex waves via FRCs. Connections at the bottom indicate the comparisons of amplitudes (A, blue) and phases (P, red) separately.

Importantly, the multislice approach calculates the wave function at the exit face of the specimen, whereas the multiplication with the object transfer function of the PO and WPO models yields the wave function in the center of the specimen if one considers the scattering process within the multislice approach for the special case with only one slice. Therefore, the waves obtained from the single-slice models were also propagated by half the specimen thickness to the specimen exit face, which we denote by PO$_{exit}$ and WPO$_{exit}$ to distinguish them from the PO and WPO models (Leidl et al., 2023).

Scattering models explored in this work are illustrated schematically in Figure 1. The subscript *exit* refers to the wave functions propagated to the specimen exit face for all models. These are complex quantities, which suggests different ways of quantitative comparisons as sketched in the lower part of Figure 1. Using the multislice result as a reference, we compare the complex simulation (black), the amplitude (blue) and the phase (red) separately. Comparisons are performed via the FRC (Saxton & Baumeister, 1982; Van Heel et al., 1982)

$$\mathrm{FRC}(k) = \frac{\sum_{|\mathbf{k}_i|\in[k,k+\Delta k)} X(\mathbf{k}_i)\cdot\overline{Y(\mathbf{k}_i)}}{\sqrt{\sum_{|\mathbf{k}_i|\in[k,k+\Delta k)} |X(\mathbf{k}_i)|^2 \sum_{|\mathbf{k}_i|\in[k,k+\Delta k)} |Y(\mathbf{k}_i)|^2}}, \tag{6}$$

where X and Y are the 2D matrices in Fourier space to be compared with each other, and $\mathbf{k}$ denotes the Fourier coordinate. $k = |\mathbf{k}|$ is the ring radius, Δk the thickness of a respective resolution shell, and $\overline{X}$ denotes the complex conjugate of X. A rectangular box 10 % larger than the protein size is used for the comparison.

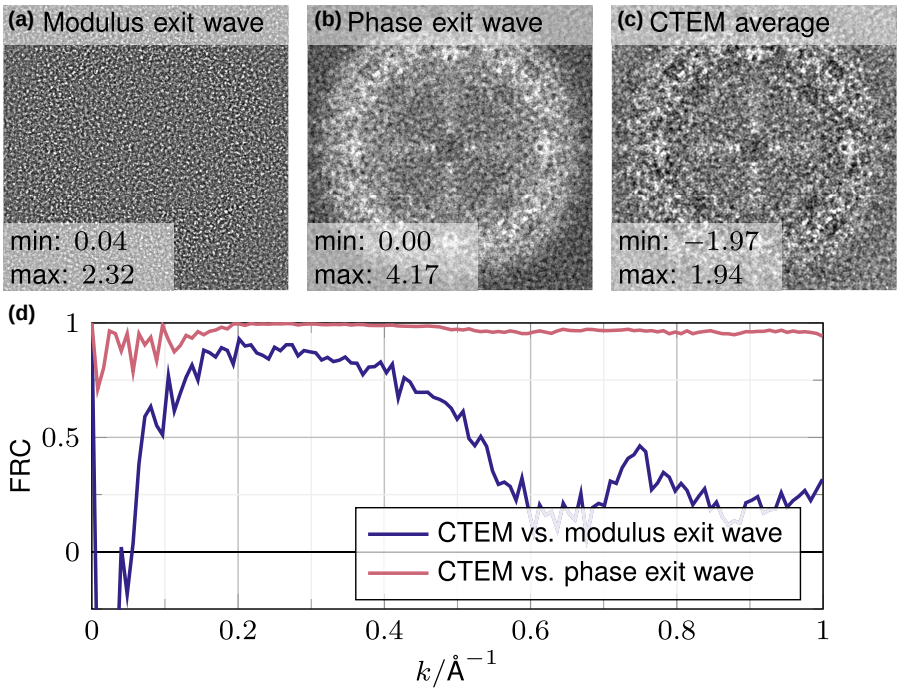

Fig. 2. Comparison of a CTEM average with the complex exit wave. (**a**/**b**) Modulus/phase of the exit wave of a multislice simulation for apoferritin. (**c**) Average of 500 inverted CTEM simulations with a randomly sampled focus between −100 nm and −1000 nm, and an infinite dose using the exit wave of the multislice simulation shown in (**a**–**b**). Before averaging, phase flips were corrected assuming the focus to be known precisely. (**d**) FRCs of the CTEM average with the amplitude and the phase of the exit wave, respectively.

For a compact analysis, the first meaningful zero of the smoothed FRC is taken as the limit of directly interpretable information transfer, being regarded as the resolution criterion Δ_{FRC} in this study. The first zero is chosen because, for higher spatial frequencies, contrast inversions occur that cannot be predicted robustly without knowing the underlying structure. Therefore, the structure is not necessarily directly interpretable at spatial frequencies beyond Δ_{FRC}. The reciprocal of Δ_{FRC} is then compared to the highest resolution published in the PDBe at the time of writing. In addition, we discuss concepts to extend the resolution beyond Δ_{FRC} (Elferich et al., 2024) further below. Note that comparing the multislice result to the WPO and PO approximations resembles the trustworthiness of interpreting experimental data within the framework of projection assumptions. Here, we focus on the exit wave functions to eliminate other resolution-limiting factors imposed by the optical system, such as aberrations and partial coherence.

Results

Phase Contrast in Average TEM Images

According to Figure 1, a total of 15 FRCs can be calculated, consisting of the comparison of five models—PO, PO_{exit}, WPO, WPO_{exit}, tWPO—each in terms of the complex exit waves, their moduli as well as their phases separately. We first address the relevance of the exit wave using apoferritin as a case study. Since the experimental observations in cryo-TEM are conventional TEM (CTEM) images acquired under various defoci, it is examined which of the signals, amplitude or phase of the exit wave, dominates the recorded image. To this end, the exit wave from the multislice simulation has been imaged on the detector 500 times, with foci distributed equally between −100 nm and −1000 nm. An infinite dose was assumed, and correction of CTF-related phase flips in the Fourier coefficients of the image intensity was performed. All TEM images were then averaged.

Figure 2a–2c shows the real-space amplitude and phase of the exit wave of the multislice simulation, as well as the average TEM image. The modulus in Figure 2a does not show significant contrast between the apoferritin particle and the LDA ice. This is different for the phase in Figure 2b, which shows a clear contrast between apoferritin and LDA ice, as well as rich structural details of apoferritin. A comparison of the phase in Figure 2b with the average TEM image in Figure 2c reveals a high similarity of both signals in real space, albeit with different contrast between the particle and the LDA ice. The FRCs in Figure 2d show a nearly perfect correlation between the average TEM image in c and the phase in b up to a resolution of 1 Å. The agreement between exit wave amplitude in Figure 2a and the average TEM image in c is significantly worse, and additionally shows a contrast inversion for low spatial frequencies at 0.06 Å^{-1}. Consequently, phase-flipped TEM images taken under large defoci rather correlate with the phase of the exit wave function than with the amplitude. Therefore, the following subsection discusses the agreement of the different scattering models as to the phases of the waves in real space.

As a side note, it is important to keep the inherent normalization contained in the FRCs in mind, i.e., the denominator of equation 6. Figure 3 shows the FRCs without normalization. For the phase, the correlation is present over the entire spatial frequency range studied here, but it is relatively low beyond 0.55 Å^{-1}. This shows that the high spatial frequencies are only faintly present in the apoferritin sample. Contrary, the FRC of the amplitude adopts a significant level mostly above the FRC of the phase between 0.3 Å^{-1} and 0.55 Å^{-1}. The amplitude is in agreement with the normalized FRCs but slightly shifted to higher frequencies.

The scattering model and imaging process are distinct entities. To ensure accurate analysis and avoid artifacts associated with CTF correction applied at the level of recorded image intensities and being is justified by analytical expressions for the WPO model only, the following sections deal with the comparison at the level of the exit waves resulting from the different scattering models.

Comparison in Real Space

Figure 4 shows the scaled projected potential σV and phases of the exit waves of the PO, $\mathrm{WPO_{exit}}$, $\mathrm{PO_{exit}}$, $\mathrm{tWPO_{exit}}$, and $\mathrm{MS_{exit}}$ simulations for the different proteins. Note that the contrast is shown at the absolute scale, normalized to the maximum contrast of each protein. All simulations show a good contrast between the proteins and the LDA ice. The contrast is nearly identical for all four simulation models for the light proteins up to TMV, whereas the total contrast decreases for σV and the $\mathrm{WPO_{exit}}$ simulations as the thickness of the proteins increases. For all thicknesses, the overall structures of the proteins are well represented by all models at least by visual inspection. However, an in-depth comparison of the resolution limit is challenging considering the real-space representations alone. Thus, the Fourier representation is used in the following, and the comparison is performed via FRCs as defined in equation (6).

Comparison in Fourier Space

Figure 5a depicts the FRCs between $\mathrm{WPO^P}$ and $\mathrm{MS^P_{exit}}$, showing oscillating behavior and attenuation with increasing spatial frequency. All proteins exhibit positive correlations except for the thickest one, which shows a contrast inversion. The first zeros of the FRCs depend on the protein and decrease systematically as the protein size increases. Thus, at least the direct interpretability of spatial frequencies within the WPO approximation is rather limited, since the correlation with the more realistic multislice simulation, which takes dynamical scattering into account, reaches up to 0.12 and 0.89 $\mathrm{Å^{-1}}$ for the largest and smallest proteins considered here, respectively.

The FRCs for the comparison between $\mathrm{WPO_{exit}}$ and $\mathrm{MS_{exit}}$ are shown in Figure 5b. Compared to the $\mathrm{WPO^P}$, the FRCs exhibit a lower oscillation frequency and, therefore, first zeros at higher spatial frequencies. For the thinnest protein, the first zero shifts from 0.89 $\mathrm{Å^{-1}}$ ($\mathrm{WPO^P}$) to 1.42 $\mathrm{Å^{-1}}$ ($\mathrm{WPO_{exit}}$), and for the capsid porcine bocavirus, from 0.42 $\mathrm{Å^{-1}}$ ($\mathrm{WPO^P}$) to 0.63 Å ($\mathrm{WPO_{exit}}$). However, the maximal value decreases even at the first resolution shells with increasing protein thickness. The FRCs of the two largest proteins show a different behavior in that their first zero shifts to significantly lower spatial frequencies as compared to the $\mathrm{WPO^P}$ counterparts in Figure 5a which points towards a breakdown of the model at comparably low spatial resolutions.

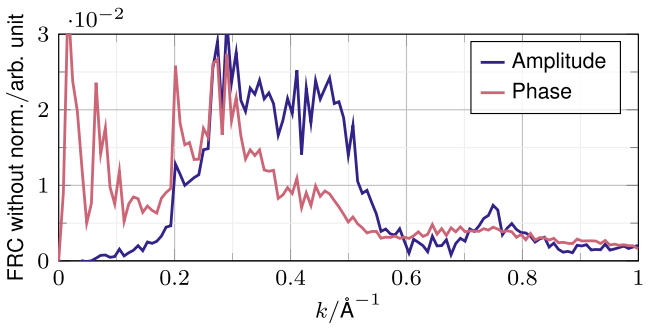

Fig. 3. FRC curves without normalization for the comparison of the CTEM average with the amplitude and phase of the exit wave. Both curves are normalized to the area under the curve, excluding the first resolution shells, for easier comparison.

Figure 5c presents the analogous evaluation for the (strong) phase object approach propagated to the exit surface $\mathrm{PO_{exit}}$. The shapes of the FRCs between the phases of the $\mathrm{PO_{exit}}$ and $\mathrm{MS_{exit}}$ are, in general, similar to Figure 5b, except that the FRCs start at one. This trend is more pronounced for thicker proteins, which can be expected since the WPO is an approximation to the PO approach for thin and/or weakly scattering specimens only. $\mathrm{PO_{exit}}$ also works reasonably well for the two thickest proteins. Compared to Figure 5a and b, the FRC of the rotavirus does not show a contrast inversion at the low spatial frequencies. This demonstrates that treating the imaging process within the phase or weak phase approximation can lead to significantly different transfer limits for the directly interpretable image contrast when thicker proteins are investigated.

Neglecting multiple scattering but accounting for the correct propagation, the tWPO model exhibits nearly constant FRCs with respect to $\mathrm{MS_{exit}}$ up to 1 $\mathrm{Å^{-1}}$, as depicted in Figure 5d. The constant value decreases with increasing protein thickness from nearly 1 to 0.22 for the 48 nm double microtubule. The largest protein the rotavirus shows a zero crossing at a frequency of 0.2 $\mathrm{Å^{-1}}$, along with a high negative correlation of approximately −0.9 for higher frequencies. The results indicate that the main effect is the correct propagation for thinner and medium-sized proteins, which is qualitatively consistent with the findings in Gureyev et al. (2020). However, multiple scattering affects the whole frequency range. For reasons of compactness, the tWPO results are not included in the following comparison in detail, since it delivers resolutions clearly below $\Delta_{\mathrm{FRC}} < 1\mathring{A}$, rather independently of the protein sizes, except for rotavirus.

In cryo-TEM, the envelope of the CTF due to thickness effects can be approximated by $\mathrm{sinc}(\pi\lambda k^2 t)$ in practice (DeRosier, 2000), where λ is the relativistic electron wavelength and t the specimen thickness. This analytical model promises the extension of the range of interpretable spatial frequencies, as currently proposed in the CTFFIND5 method (Elferich et al., 2024). Mathematically, the first zero of the sinc corresponds to a spatial frequency of $(\lambda t)^{-1/2}$, which is a phase shift of π due to the defocus term $\pi\lambda a|k|^2$ between the entrance and exit surface. The sinc functions for the different protein thicknesses are shown in Figure 5e. They agree rather well with Δ_{FRC} comparing $\mathrm{WPO^P}$ to $\mathrm{MS^P_{exit}}$ in Figure 5a. As in Figure 5a, they resemble a similar oscillatory behavior in qualitative respect. Differences are observed before the first zero, and slightly higher maxima are present for the $\mathrm{WPO^P}$ case. Furthermore, a contrast inversion is observed in Figure 5a for the largest protein (rotavirus), which is not the case for the sinc function in Figure 5e.

Scattering Model Dependent Resolution for Directly Interpretable Image Contrast and Comparison to Experimental Data

The first zeros of the smoothed FRCs yield the maximum spatial frequencies Δ_{FRC} up to which the image contrast is

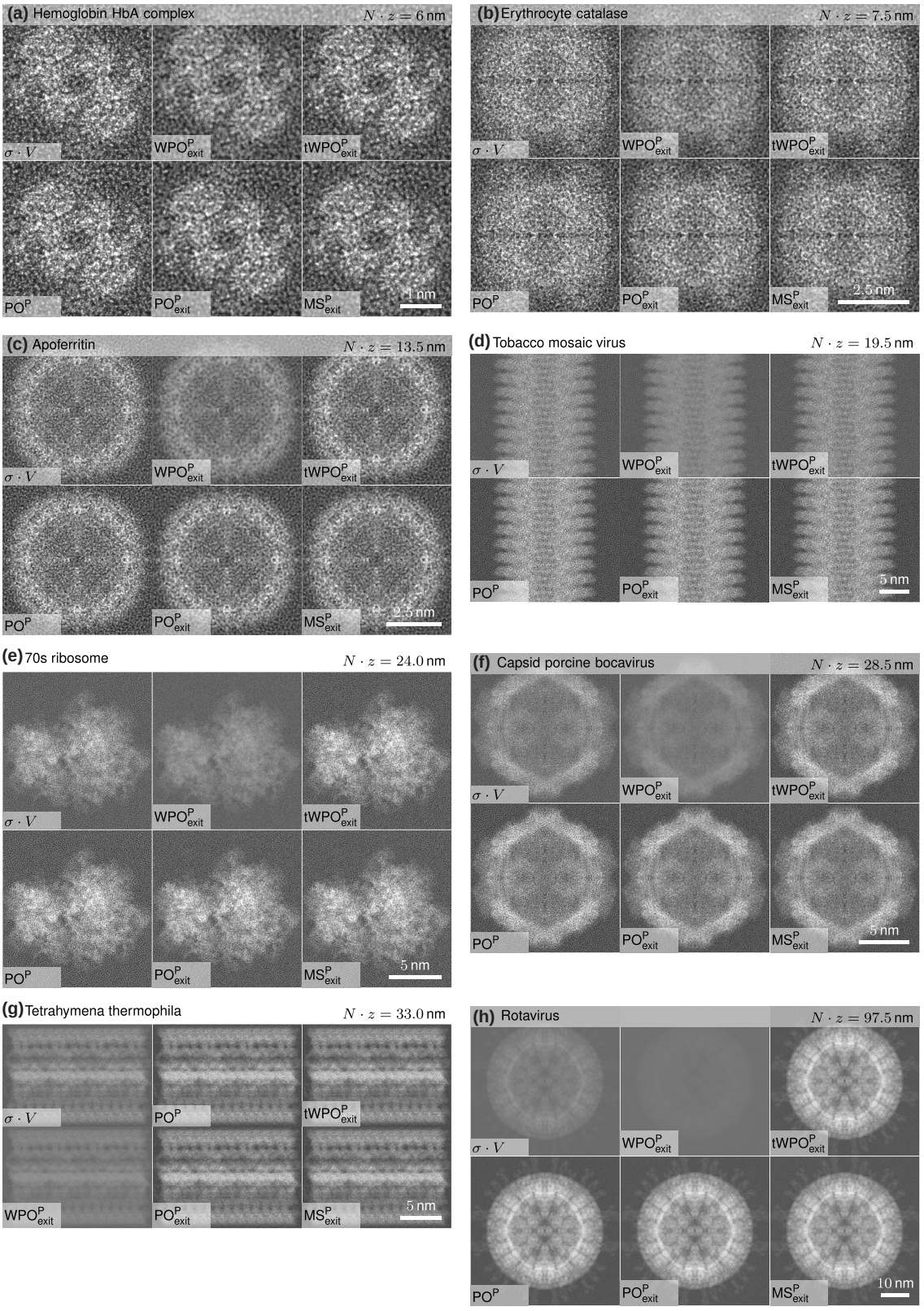

Fig. 4. Real-space comparison of the single-slice models with the multislice simulation based on the phase. Starting from the top left, the scaled projected potential followed by phases as obtained from the $\mathrm{WPO}_{\mathrm{exit}}$, tWPO, PO, $\mathrm{PO}_{\mathrm{exit}}$, and the full $\mathrm{MS}_{\mathrm{exit}}$ simulation are shown. The proteins (**a**–**h**) are ordered by their thickness, as indicated by the label, in the projection direction from thinnest to thickest. The contrast is normalized to the maximum contrast for each protein.

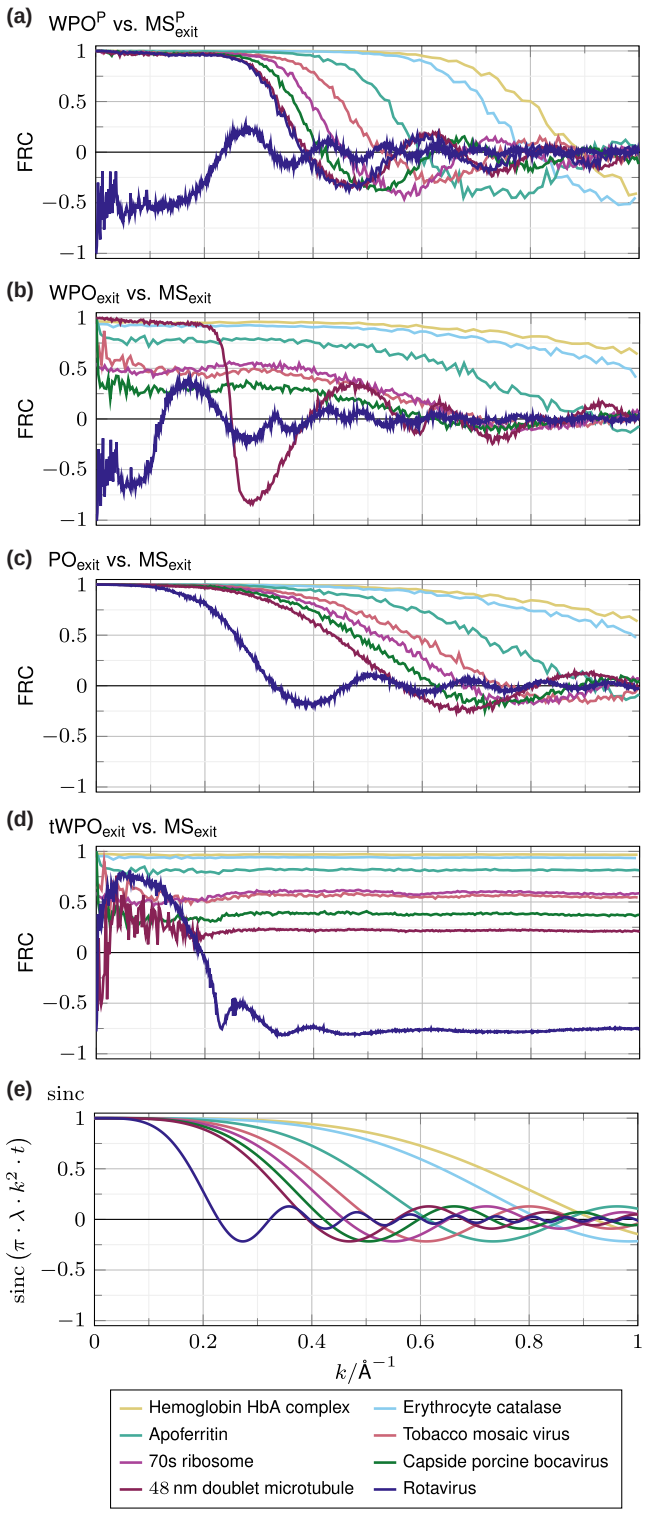

Fig. 5. Comparison of the phase of the single-slice models propagated to the exit surface with the multislice simulation via FRCs. (**a**/**b**) FRC between the phase of WPO_{exit}/PO_{exit} and the phase of the MS_{exit} simulation. (**c**) FRC between complex valued WPO_{exit} and MS_{exit}. (**d**) FRC between complex $tWPO_{exit}$ and MS_{exit} for the three thickest proteins. (**e**) sinc for the different protein thicknesses.

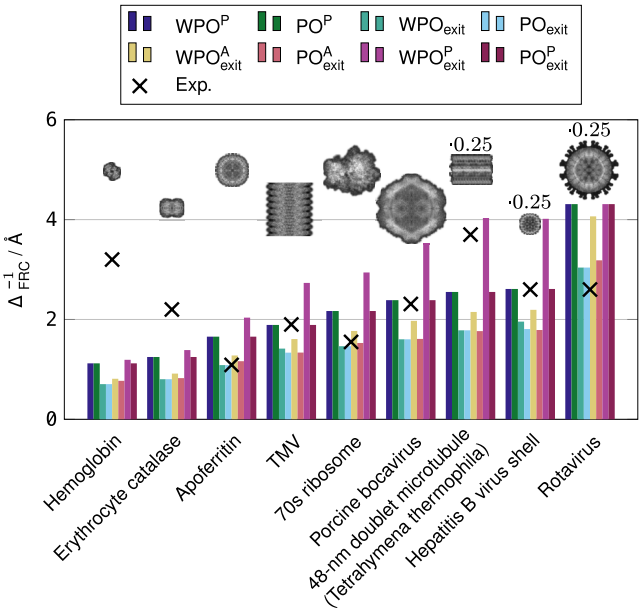

Fig. 6. Comparison of the maximal reachable resolutions by single-slice models using the first zero of the FRC curves between the different single-slice models and the multislice simulation (Δ_{FRC}). The superscripts A and P stand for a separate comparison of the real-space amplitude and phase. On top, each protein is shown in vacuum in projection direction with the correct relative scaling. The exceptions are the large proteins of Tetrahymena thermophila, the Hepatitis B virus shell and the rotavirus, whose sizes are reduced by a factor of 0.25.

expected to be directly interpretable in terms of a projection of the structures using the single-scattering approaches. Because only a single number is now representing the applicability of the different scattering models (instead of the full FRC curves as in Fig. 5), further comparisons of complex wave functions, amplitudes and phases according to Figure 1 are now presentable in very compact manner. The comparison of the amplitudes shows the first zero close to the origin, such that we used the zero after the first plateau as a resolution criterion. Comparisons to experiments have been carried out using the highest resolution reported in the literature for the proteins of interest here, as listed in Table 1. For apoferritin, the resolution benchmark was taken as 1.09 Å (Küçükoğlu et al., 2024) and for the rotavirus as 2.6 Å (Grant & Grigorieff, 2015).

The maximum resolutions are shown in Figure 6 for all models from Figure 1 as a series of bars for each protein, whereas the crosses indicate the current experimental resolution benchmark from literature. Note that we distinguish results according to single-scattering models (W)PO in that wave functions in the slice center and at the exit face of the specimen are treated separately, the latter marked by the subscript *exit*. The superscripts *A* and *P* refer to the FRCs of either amplitude or phase, respectively, with the counterpart from the multislice simulation.

The global trend in Figure 6 is rather similar for most scattering models. Since the proteins are ordered by their size horizontally, the theoretical resolution gradually decreases from values slightly better than 1 Å in the case of hemoglobin to only 3 Å for the rotavirus. Note that the insets depict the proteins at correct relative sizes, except for the scaling by a factor of 0.25 for the largest three ones. For all simulated proteins, the lower bound is given by PO_{exit} (represented by bright blue bars). Note again that the term *resolution* refers to the correlation with the multislice result, which serves as a proxy for the spatial frequency distribution of the signal that an ideal experiment can achieve. All scattering models that are

compared in Figure 6 exploit the projection assumption and, therefore, represent the idealized cryo-TEM imaging. For this reason, we omitted the results of the tWPO model from the plot, as it interweaves depth-dependent scattering and propagation to form an exit wave that differs significantly from a structurally faithful projection. A correlation with the multislice result rather indicates the extent to which the complex interaction with the specimen can be approximated by the tWPO approach in equation (3) than elucidating the direct structural interpretability of the tWPO result.

It is instructive to compare the theoretical predictions of the resolutions in Figure 6 with the experimental resolution benchmarks from the literature, as found at the time of writing. For apoferritin and larger proteins, the predictions are in relatively good agreement with the experiments. The 48 nm doublet microtubule constitutes an outlier where the experimental resolution is approximately 2 Å worse than predicted. This may originate from the uncommon geometry and high flexibility of the molecule, or indicate further potential for improving the resolution. A more stable protein, the Hepatitis B virus core shell, was resolved to 2.6 Å, 1 Å better than the 48 nm double microtubule. The shell, with a diameter of 35 nm, is slightly larger than the 48 nm doublet microtubule, and was recorded using a modern Quantum-K2 detector (Böttcher & Nassal, 2018). It is closer to the simulated resolutions, with a deviation of 0.8 Å to Δ_{FRC}. For the rotavirus, the experimental resolution is slightly better than the Δ_{FRC} of PO_{exit} by 0.4 Å. Possible explanations include the high symmetry of C60, which is enforced during single-particle reconstructions. Each symmetric unit has a size of only 27.5 nm in the radial direction, compared to a total projection thickness of 97.5 nm. Other explanations include the varying ice-to-protein ratio in the z-direction and the fact that the LDA ice is averaged out during single-particle reconstruction, which is not the case for the presented simulations.

The situation is different for small proteins, such as the 6 nm thick hemoglobin and the 7.5 nm thick erythrocyte catalase. From the perspective of the reliability of scattering models employing the projection assumption, the smallest proteins should be resolvable at the sub-Angstrom level. In contrast, the experimental data imply a trend of deteriorating resolution with decreasing protein size. Several plausible explanations can account for this effect. Firstly, these proteins cause very small phase shifts of the incident electron wave, which translates to much lower contrast in experimental cryo-TEM images and is furthermore a potential source of inaccurate alignments in single-particle reconstructions. Secondly, the thickness of the LDA ice in cryo-TEM is a crucial parameter. The too optimistic resolution limit predicted by theory here could also stem from our assumption of an ice layer with a thickness approximately equal to that of the protein itself. In experiments, this may be different, such that the resolution of hemoglobin and erythrocyte catalase is limited by a lower thickness limit of LDA ice, which is thicker than the protein size, resulting in increased structural noise. On a more speculative note, the perfect agreement between experimental and theoretical resolution for apoferritin might indicate that ice thicknesses around the diameter of this protein are a lower limit for reproducible specimen preparation with current plunge-freezing practice. This is consistent with tomographic measurements of the ice thickness for apoferritin with a minimal ice thickness of 20 nm (Brown & Hanssen, 2022). As previously discussed, the additional ice, 0.8 or 2.3 times the specimen thickness of TMV, has a noticeable effect on dynamic scattering. It reduces the FRCs over a broad frequency range down to 0.75 or 0.5 (Leidl et al., 2023).

Discussion

Considering the complexity of modeling the freezing process and the dynamical scattering at the atomic level, and the rather crude condensation of the complicated spatial frequency dependence of the FRC curves to a single number (Δ_{FRC}) to estimate the attainable resolution for projection assumptions PO and WPO, the good agreement with experimental resolution benchmarks in Figure 6 beyond apoferritin indicates two conclusions. Firstly, contemporary multislice simulations, combined with molecular dynamics, are reliable concepts for the quantitative interpretation of cryo-TEM data. The correspondence between PO and WPO approximations and a full multislice result for the specimen exit wave function vanishes at spatial frequencies nearly identical to the maximum frequencies obtained experimentally, employing essentially the same approximations during data processing. Considering the numerous challenges cryo-TEM data acquisition and processing face, this is remarkable because Figure 6 implies that single-particle cryo-TEM resolution is currently limited by the scattering model used to map a 3D protein model onto experimental images. For the deterioration of the experimental resolution of the smaller proteins, erythrocyte catalase and hemoglobin, which disagrees with the thickness-dependent resolution trend predicted by our simulations, a lower limit for the ice thickness can only serve as part of the explanation. In this case, a stagnation of the resolution would be expected since all specimens with proteins smaller than apoferritin should instead adopt identical ice thicknesses. Here, the low contrast against the structural noise and the challenge of determining the exact location of a protein within the ice, both laterally and in electron beam direction (defocus), play a potentially crucial role.

Secondly, the indication that projection assumptions during 3D single-particle reconstructions constitute a limit to spatial resolution for large proteins might stimulate the exploration of more accurate approaches to map a 3D model to the respective experimental 2D cryo-TEM images. In this respect, the nearly perfect agreement between the first zero crossings of the protein-thickness-dependent sinc function (Elferich et al., 2024) and Δ_{FRC} in Figure 5 indicates that including a respective correction of the contrast inversions of the single-slice models to current CTF correction schemes promises a further improvement. However, note that rotationally symmetric corrections in Fourier space would not alter the absolute values of the FRCs by definition, but mitigate the phase flips.

The characteristic trend of the theoretically attainable resolution in Figure 6 with respect to specimen thickness suggests a quantitative analysis of the thickness-dependent theoretical resolution limit, which is presented in Figure 7. For most proteins, the best resolution is provided by WPO_{exit} and PO_{exit}, which are nearly identical in Δ_{FRC}. Therefore, we focus on PO_{exit} and the simple projection PO^{P}, which are represented by light blue crosses and green stars in Figure 7.

Importantly, it is observed that the theoretical resolution limit shows a proportionality to the square root of the protein thickness, such that the horizontal axis in Figure 6 is scaled as $\sqrt{t}$. A linear fit to the PO^{P} and PO_{exit} data has been performed, resulting in the solid lines and fit coefficients shown in the inset. At least for these approximations and the resolution

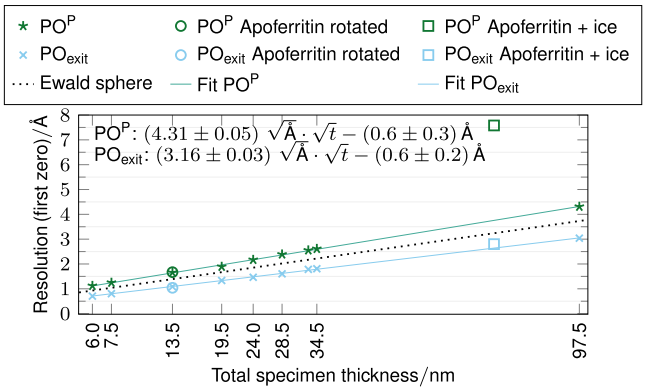

Fig. 7. Dependence of the attainable resolution using single-slice models on projection thickness. First zeros of the FRC between the multislice simulation and the PO^P as well as the PO_{exit} model were used as criteria. For the horizontal t-axis, a square root scaling is used. The fit parameters of a linear fit to $\sqrt{t}$ are given top left, where t is assumed in Å. The green (top) and light blue (bottom) circles mark Δ_{FRC} for a rotated apoferritin, and the squares represent ΔFRC for apoferritin with 60 nm additional ice below for the models PO^P and PO_{exit}.

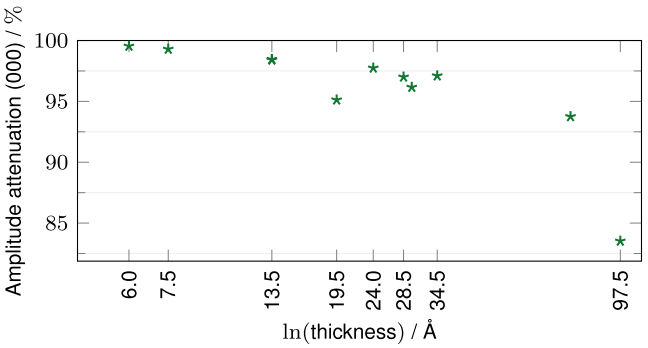

Fig. 8. Attenuation of the undiffracted beam amplitude. To assess the impact of nonlinear imaging that involves the mutual interference of scattered beams, this graph shows the protein size dependent amplitude of the undiffracted beam from multislice simulations, in terms of the fraction of its amplitude when entering the specimen.

criterion Δ_{FRC}, the fits can serve as a reference point for the attainable experimental resolution of further structures. Note that the linear fits have been performed unconstrained, such that they do not pass exactly through the origin. However, the origin is well contained within three times the confidence intervals given by the error of the intercept with the resolution axis. Of course, the analysis solely refers to simplified scattering models used to interpret experimental observations and neglects aspects of structural variability and flexibility of the molecules under study. The dotted line in Figure 7 represents the separation of resolution regimes, where the Ewald sphere correction can be neglected (above the dotted line) or needs to be taken into account (below the dotted line), according to the criteria proposed by DeRosier (2000). This line expresses a recommendation for cryo-TEM data processing strategies rather than a resolution limit.

A simulation of apoferritin rotated by 1.4142°, 3.1415°, and 1.7320° with a projection thickness of 13.5 nm is added to Figure 7 (circles), showing that Δ_{FRC} is nearly unaffected for both models (PO^P and PO_{exit}) for a round symmetric protein. In addition, an apoferritin simulation with an additional 60 nm LDA ice below shows a Δ_{FRC} value slightly above the linear fit for the PO_{exit}. However, PO^P exhibits a significantly worse resolution than the linear fit would suggest, which can be attributed to the maximum distance of the protein from the exit surface.

Working out limitations to treating the specimen as a weak scatterer is furthermore connected to treating the imaging process as linear or nonlinear, respectively. A detailed study of the nonlinear contributions is beyond the scope of the present work, so only a few aspects shall be mentioned here. In cases where the unscattered beam amplitude cannot be considered large compared to the scattered ones, the imaging process including partial coherence is described in terms of transmission cross coefficients (Ishizuka, 1980; Coene et al., 1996; Krause et al., 2013; Chang et al., 2017; Chen & Ge, 2021) (TCCs), which additionally take the mutual interferences among all scattered beams into account. Figure 8 shows the amplitude of the unscattered beam for all simulated proteins as a function of the natural logarithm of the projection thickness ($N \cdot z$). Nearly all proteins exhibit an attenuation of the primary beam amplitude of less than 10 %. For the rotavirus with a thickness of 97.5 nm, the attenuation increases to 16.5 %. Scattered amplitudes make up to 10 % of this value, i.e., up to 1.6 % of the total signal in the diffraction plane. Given the nearly linear falloff of the logarithm of the power spectrum of the specimen exit wave across spatial frequencies, several nonzero cross-terms can be expected, resulting in a computationally demanding but potentially important consideration of TCC.

Summary and Outlook

The first zero of the FRC curves between a full dynamical simulation and projection-based scattering models shows a square root dependence on the specimen thickness. This trend corresponds quantitatively to the experimentally reported resolutions for proteins with the size of apoferritin or larger. Theoretical resolutions between 0.7 Å and 3 Å to 4 Å are found for 6 nm thick hemoglobin and 97.5 nm thick rotavirus, respectively. This is sufficient to resolve, e.g., α-helices and β-sheets in all cases. Our results suggest that it is essential to be aware of underlying scattering model assumptions in cryo-TEM processing, currently based on the (weak) phase approximation in single-particle reconstructions, in order to achieve higher resolutions for stable proteins in the future. As the results suggest the main effect being propagation, an efficient approximation to the multislice method, modeling the interaction by single, but depth-dependent, weak scattering in terms of the tWPO approach at the level of wave functions, is expected to readily and reliably include high spatial frequencies up to at least $1\,Å^{-1}$, also for specimens with a thickness of many tens of nanometres.

From a more general perspective, the wealth of available experimental data in single-particle cryo-TEM may enable the application of more accurate reconstructions, which could be subsequently incorporated into the current workflow to refine the 3D density by employing a few-slice multislice model or using the tWPO scheme as a reliable and computationally less demanding approximation. According to Figure 5d, the tWPO model shows very high Fourier shell correlations with the multislice model. However, for the nearly 97.5 nm thick rotavirus, the tWPO model suffers from a nonideal low spatial frequency transfer. This suggests using the current projection-based method to recover the low spatial frequencies and then using tWPO for subsequently refining the high spatial frequencies. In analogy to electron ptychography (Hoppe, 1969 ; Maiden & Rodenburg, 2009; Chen et al., 2021), currently developing within the field of cryo-scanning TEM (Leidl et al.,

2023; Küçükoğlu et al., 2024), gradient-based schemes (Van den Broek & Koch, 2012) might well be suited to update the 3D model slice-wise, as done in tomography where this is termed "sequential reconstruction & joint alignment" (You et al., 2024). Note that Fourier-ptychographic measurements based on reciprocity between conventional and scanning TEM can also be used to reconstruct the complex object (Lorenzen et al., 2024), such that the ptychographic method is readily applicable to cryo-TEM imaging also in the absence of momentum-resolved scanning TEM capabilities.

Obviously the exploitation of the more complex multiple scattering models in forward direction poses severe challenges for solving the inverse problem in cryo-TEM as to prevalent reconstruction workflows, on the one hand. On the other hand, inverse multislice combined with momentum-resolved scanning TEM established as a routine approach in materials science owing to the recent detector and computational hardware development. Clearly the application of respective workflows to cryo-TEM involves major challenges far beyond sole software-related implementation, because the stability of inverse problem solvers in the presence of Poisson noise at low doses is vastly unexplored. However, the imaging of thick proteins or cross-sections of cells might render further developments in this direction useful. Moreover, the reliability of single-scattering models, especially of the weak phase approximation, scales with the interaction constant σ. Since it increases with decreasing acceleration voltage of the TEM, low-voltage cryo-TEM might suffer spatial resolution already at medium-size proteins, if data is interpreted and processed in terms of kinematic scattering.

In this work, a substantial computational effort has been made to simulate elastic dynamical scattering in LDA ice-embedded proteins using atomistic models, neglecting spatial and temporal coherence envelopes. Although inelastic scattering, e.g., due to exciting core states or plasmons, becomes significant in specimens with thicknesses of a few tens of nanometers, this study is nevertheless of direct practical relevance for zero-energy-loss filtered cryo-TEM imaging or cryo-TEM employing a corrector for chromatic aberration. All analyses dealt with 2D images. Simulating a multitude of images for different foci and incident beam directions, and subjecting them to a typical 3D protein reconstruction workflow to obtain, e.g., local resolution maps with the 3D structure of the ground truth known, is left as a future task. This is also suggested to address so far neglected effects such as the filling factor of the protein, the beam-induced Brownian motion of the particles in ice, as well as the motion of the water molecules in the LDA ice, which is different from the protein under electron irradiation (McMullan et al., 2015; Himes & Grigorieff, 2021).

Availability of Data and Materials

The authors have declared that no datasets apply for this piece.

Acknowledgments

The authors acknowledge funding from the European Research Council within the Horizon Europe innovation funding programme under Grant Agreement 101118656 (ERC Synergy project 4D-BioSTEM).

Financial Support

The current study hasn't received any fund from any organizations or institutions.

Conflict of Interest

The authors declare no conflicts of interest.

References

Armstrong DR, Berrisford JM, Conroy MJ, Gutmanas A, Anyango S, Choudhary P, Clark AR, Dana JM, Deshpande M, Dunlop R, Gane P, G'aborov'a R, Gupta D, Haslam P, Koca J, Mak L, Mir S, Mukhopadhyay A, Nadzirin N, Nair S, Paysan-Lafosse T, Pravda L, Sehnal D, Salih O, Smart O, Tolchard J, Varadi M, Svobodova-Varekov'a R, Zaki H, Kleywegt GJ & Velankar S (2020). Pdbe: Improved findability of macromolecular structure data in the pdb. *Nucleic Acids Res* **48**, D335–D343. https://doi.org/10.1093/nar/gkz990

Aston-Deaville S, Carlsson E, Saleem M, Thistlethwaite A, Chan H, Maharjan S, Facchetti A, Feavers IM, Siebert CA, Collins RF, Roseman A & Derrick JP (2020). An assessment of the use of Hepatitis B Virus core protein virus-like particles to display heterologous antigens from *Neisseria meningitidis*. *Vaccine* **38**(16), 3201–3209. https://doi.org/10.1016/j.vaccine.2020.03.001

Böttcher B & Nassal M (2018). Structure of mutant hepatitis B core protein capsids with premature secretion phenotype. *J Mol Biol* **430**(24), 4941–4954. https://doi.org/10.1016/j.jmb.2018.10.018

Brown HG & Hanssen E (2022). Measureice: Accessible on-the-fly measurement of ice thickness in cryo-electron microscopy. *Commun Biol* **5**(1), 817. https://doi.org/10.1038/s42003-022-03698-x

Chang Y, Li S, Wang Y & Ge B (2017). Applicability of non-linear imaging in high-resolution transmission electron microscopy. *Microscopy* **66**, 406–413. https://doi.org/10.1093/jmicro/dfx031

Chen M & Ge B (2021). Further discussion on the separation of linear and nonlinear components in hrtem imaging. *Micron* **145**(6), 103054. https://doi.org/10.1016/j.micron.2021.103054

Chen Z, Jiang Y, Shao YT, Holtz ME, Odstrčil M, Guizar-Sicairos M, Hanke I, Ganschow S, Schlom DG & Muller DA (2021). Electron ptychography achieves atomic-resolution limits set by lattice vibrations. *Science* **372**(6544), 826–831. https://doi.org/10.1126/science.abg2533

Chen S, Li J, Vinothkumar KR & Henderson R (2022). Interaction of human erythrocyte catalase with air–water interface in cryoem. *Microscopy* **71**(Supplement_1), i51–i59. https://doi.org/10.1093/jmicro/dfab037

Coene WMJ, Thust A, Op de Beeck M & van Dyck D (1996). Maximum-likelihood method for focus-variation image reconstruction in high resolution transmission electron microscopy. *Ultramicroscopy* **64**(1-4), 109–135. https://doi.org/10.1016/0304-3991(96)00010-1

Cowley JM & Moodie AF (1957). The scattering of electrons by atoms and crystals. I. A new theoretical approach. *Acta Crystallogr* **10**(10), 609–619. https://doi.org/10.1107/S0365110X57002194

Cowley JM & Moodie AF (1959*a*). The scattering of electrons by atoms and crystals. II. The effects of finite source size. *Acta Crystallogr* **12**(5), 353–359. https://doi.org/10.1107/S0365110X59001098

Cowley JM & Moodie AF (1959*b*). The scattering of electrons by atoms and crystals. III. Single-crystal diffraction patterns. *Acta Crystallogr* **12**(5), 360–367. https://doi.org/10.1107/S0365110X59001104

DeRosier DJ (2000). Correction of high-resolution data for curvature of the Ewald sphere. *Ultramicroscopy* **81**(2), 83–98. https://doi.org/10.1016/S0304-3991(99)00120-5

Elferich J, Kong L, Zottig X & Grigorieff N (2024). CTFFIND5 provides improved insight into quality, tilt and thickness of TEM samples. *Elife* **13**, RP97227. https://doi.org/10.7554/eLife.97227

Faruqi A & McMullan G (2018). Direct imaging detectors for electron microscopy. *Nucl Instrum Methods Phys Res A* **878**(1), 180–190. https://doi.org/10.1016/j.nima.2017.07.037

Fromm SA, O'Connor KM, Purdy M, Bhatt PR, Loughran G, Atkins JF, Jomaa A & Mattei S (2023). The translating bacterial ribosome at 1.55 å resolution generated by cryo-EM imaging services. *Nat Commun* **14**(1), 1095. https://doi.org/10.1038/s41467-023-36742-3

Goodman JW (2005). *Introduction to Fourier Optics*. Greenwood Village, CO: Roberts and Company Publishers.
Grant T & Grigorieff N (2015). Measuring the optimal exposure for single particle cryo-EM using a 2.6 å reconstruction of rotavirus VP6. *Elife* **4**, e06980. https://doi.org/10.7554/eLife.06980
Gureyev T, Quiney H, Kozlov A & Allen L (2020). Relative roles of multiple scattering and fresnel diffraction in the imaging of small molecules using electrons. *Ultramicroscopy* **218**, 113094. https://doi.org/10.1016/j.ultramic.2020.113094
Himes B & Grigorieff N (2021). Cryo-tem simulations of amorphous radiation-sensitive samples using multislice wave propagation. *IUCrJ* **8**(6),943–953. https://doi.org/10.1107/S2052252521008538
Hoppe W (1969). Beugung im inhomogenen Primärstrahlwellenfeld. I. Prinzip einer Phasenmessung von Elektronenbeungungsinterferenzen. *Acta Crystallogr Sec A* **25**(4), 495–501. https://doi.org/10.1107/S0567739469001045
Ishizuka K (1980). Contrast transfer of crystal images in TEM. *Ultramicroscopy* **5**(1-3), 55–65. https://doi.org/10.1016/0304-3991(80)90011-X
Kabius B, Hartel P, Haider M, Müller H, Uhlemann S, Loebau U, Zach J & Rose H (2009). First application of cc-corrected imaging for high-resolution and energy-filtered tem. *J Electron Microsc (Tokyo)* **58**(3), 147–155. https://doi.org/10.1093/jmicro/dfp021
Khoshouei M, Radjainia M, Baumeister W & Danev R (2017). Cryo-em structure of haemoglobin at 3.2 å determined with the volta phase plate. *Nat Commun* **8**(1), 16099. https://doi.org/10.1038/ncomms16099
Krause FF, Müller K, Zillmann D, Jansen J, Schowalter M & Rosenauer A (2013). Comparison of intensity and absolute contrast of simulated and experimental high-resolution transmission electron microscopy images for different multislice simulation methods. *Ultramicroscopy* **134**, 94–101. https://doi.org/10.1016/j.ultramic.2013.05.015
Kubo S, Black CS, Joachimiak E, Yang SK, Legal T, Peri K, Khalifa AAZ, Ghanaeian A, McCafferty CL, Valente-Paterno M, De Bellis C, Huynh PM, Fan Z, Marcotte EM, Wloga D & Bui KH (2023). Native doublet microtubules from tetrahymena thermophila reveal the importance of outer junction proteins. *Nat Commun* **14**(1), 2168. https://doi.org/10.1038/s41467-023-37868-0
Küçükoğlu B, Mohammed I, Guerrero-Ferreira RC, Ribet SM, Varnavides G, Leidl ML, Lau K, Nazarov S, Myasnikov A, Kube M, Radecke J, Sachse C, Müller-Caspary K, Ophus C & Stahlberg H (2024). Low-dose cryo-electron ptychography of proteins at sub-nanometer resolution. *Nat Commun* **15**(1), 8062. https://doi.org/10.1038/s41467-024-52403-5
Leidl ML, Sachse C & Müller-Caspary K (2023). Dynamical scattering in ice-embedded proteins in conventional and scanning transmission electron microscopy. *IUCrJ* **10**(4), 475–486. https://doi.org/10.1107/S2052252523004505
Lobato I & Van Dyck D (2014). An accurate parameterization for scattering factors, electron densities and electrostatic potentials for neutral atoms that obey all physical constraints. *Acta Crystallogr A Found Adv* **70**(6), 636–649. https://doi.org/10.1107/S205327331401643X
Lorenzen T, März B, Xue T, Beyer A, Volz K, Bein T & Müller-Caspary K (2024). Imaging built-in electric fields and light matter by Fourier-precession TEM. *Sci Rep* **14**(1), 1320. https://doi.org/10.1038/s41598-024-51423-x
Maiden AM & Rodenburg JM (2009). An improved ptychographical phase retrieval algorithm for diffractive imaging. *Ultramicroscopy* **109**(10), 1256–1262. https://doi.org/10.1016/j.ultramic.2009.05.012
McMullan G, Vinothkumar K & Henderson R (2015). Thon rings from amorphous ice and implications of beam-induced brownian motion in single particle electron cryo-microscopy. *Ultramicroscopy* **158**(3), 26–32. https://doi.org/10.1016/j.ultramic.2015.05.017
Nakane T, Kotecha A, Sente A, McMullan G, Masiulis S, Brown PM, Grigoras IT, Malinauskaite L, Malinauskas T, Miehling J, Uchanski T, Yu L, Karia D, Pechnikova EV, de Jong E, Keizer J, Bischoff M, McCormack J, Tiemeijer P, Hardwick SW, Chirgadze DY, Murshudov G, Aricescu AR & Scheres SHW (2020). Single-particle cryo-EM at atomic resolution. *Nature* **587**(7832), 152–156. https://doi.org/10.1038/s41586-020-2829-0
Punjani A, Rubinstein JL, Fleet DJ & Brubaker MA (2017). cryoSPARC: Algorithms for rapid unsupervised cryo-EM structure determination. *Nat Methods* **14**(3), 290–296. https://doi.org/10.1038/nmeth.4169
Rohou A & Grigorieff N (2015). Ctffind4: Fast and accurate defocus estimation from electron micrographs. *J Struct Biol* **192**(2), 216–221. https://doi.org/10.1016/j.jsb.2015.08.008
Saxton W & Baumeister W (1982). The correlation averaging of a regularly arranged bacterial cell envelope protein. *J Microsc* **127**(2), 127–138. https://doi.org/10.1111/jmi.1982.127.issue-2
Seki T, Takanashi N & Abe E (2018). Integrated contrast-transfer-function for aberration-corrected phase-contrast STEM. *Ultramicroscopy* **194**, 193–198. https://doi.org/10.1016/j.ultramic.2018.08.008
Settembre EC, Chen JZ, Dormitzer PR, Grigorieff N & Harrison SC (2011). Atomic model of an infectious rotavirus particle. *EMBO J* **30**(2), 408–416. https://doi.org/10.1038/emboj.2010.322
Shang Z & Sigworth FJ (2012). Hydration-layer models for cryo-EM image simulation. *J Struct Biol* **180**(1), 10–16. https://doi.org/10.1016/j.jsb.2012.04.021
Thompson AP, Aktulga HM, Berger R, Bolintineanu DS, Brown WM, Crozier PS, in't Veld PJ, Kohlmeyer A, Moore SG, Nguyen TD, Shan R, Stevens MJ, Tranchida J, Trott C & Plimpton SJ, 2022). Lammps-a flexible simulation tool for particle-based materials modeling at the atomic, meso, and continuum scales. *Comput Phys Commun* **271**(4), 108171. https://doi.org/10.1016/j.cpc.2021.108171
Urban KW (2008). Studying atomic structures by aberration-corrected transmission electron microscopy. *Science* **321**(5888), 506–510. https://doi.org/10.1126/science.1152800
Van den Broek W & Koch CT (2012). Method for retrieval of the three-dimensional object potential by inversion of dynamical electron scattering. *Phys Rev Lett* **109**(24), 245502. https://doi.org/10.1103/PhysRevLett.109.245502
Van Heel M, Keegstra W, Schutter W & Van Bruggen E (1982). Arthropod hemocyanin structures studied by image analysis. *Life Chem Rep Suppl* **1**, 5.
Velez M, Mietzsch M, Hsi J, Bell L, Chipman P, Fu X & McKenna R (2023). Structural characterization of canine minute virus, rat and porcine bocavirus. *Viruses* **15**(9), 1799. https://doi.org/10.3390/v15091799
Weis F, Beckers M, von Der Hocht I & Sachse C (2019). Elucidation of the viral disassembly switch of tobacco mosaic virus. *EMBO Rep* **20**(11), e48451. https://doi.org/10.15252/embr.201948451
Yip KM, Fischer N, Paknia E, Chari A & Stark H (2020). Atomic-resolution protein structure determination by cryo-EM. *Nature* **587**(7832), 157–161. https://doi.org/10.1038/s41586-020-2833-4
You S, Romanov A & Pelz P (2024). 'Near-isotropic sub-Ångstrom 3D resolution phase contrast imaging achieved by end-to-end ptychographic electron tomography.' arXiv, arXiv:2407.19407, preprint: not peer reviewed https://doi.org/10.48550/arXiv.2407.19407
Zivanov J, Nakane T & Scheres SH (2019). A Bayesian approach to beam-induced motion correction in cryo-EM single-particle analysis. *IUCrJ* **6**(1), 5–17. https://doi.org/10.1107/S205225251801463X
Zivanov J, Nakane T & Scheres SH (2020). Estimation of high-order aberrations and anisotropic magnification from cryo-EM data sets in relion-3.1. *IUCrJ* **7**(2), 253–267. https://doi.org/10.1107/S2052252520000081